The Astrophysical Journal, 959:95 (12pp), 2023 December 20 https://doi.org/10.3847/1538-4357/acfd95
© 2023. The Author(s). Published by the American Astronomical Society.
OPEN ACCESS

JWST NIRCam Observations of SN 1987A: Spitzer Comparison and Spectral Decomposition

Richard G. Arendt[1,2,3], Martha L. Boyer[4], Eli Dwek[2], Mikako Matsuura[5], Aravind P. Ravi[6], Armin Rest[4,7], Roger Chevalier[8], Phil Cigan[9], Ilse De Looze[10], Guido De Marchi[11], Claes Fransson[12], Christa Gall[13], R. D. Gehrz[14], Haley L. Gomez[5], Tuomas Kangas[15,16], Florian Kirchschlager[10], Robert P. Kirshner[17], Josefin Larsson[18], Peter Lundqvist[19], Dan Milisavljevic[20], Sangwook Park[6], Nathan Smith[21], Jason Spyromilio[22], Tea Temim[23], Lifan Wang[24], J. Craig Wheeler[25], and Charles E. Woodward[14]

[1] Center for Space Sciences and Technology, University of Maryland, Baltimore County, Baltimore, MD 21250, USA; Richard.G.Arendt@nasa.gov
[2] Code 665, NASA/GSFC, 8800 Greenbelt Road, Greenbelt, MD 20771, USA
[3] Center for Research and Exploration in Space Science and Technology, NASA/GSFC, Greenbelt, MD 20771, USA
[4] Space Telescope Science Institute, 3700 San Martin Drive, Baltimore, MD 21218, USA
[5] School of Physics and Astronomy, Cardiff University, Queen's Buildings, The Parade, Cardiff CF24 3AA, UK
[6] Department of Physics, University of Texas at Arlington, Box 19059, Arlington, TX 76019, USA
[7] Department of Physics and Astronomy, The Johns Hopkins University, Baltimore, MD 21218, USA
[8] Department of Astronomy, University of Virginia, P.O. Box 400325, Charlottesville, VA 22904-4325, USA
[9] U.S. Naval Observatory, 3450 Massachusetts Avenue N.W., Washington, DC 20392-5420, USA
[10] Sterrenkundig Observatorium, Ghent University, Krijgslaan 281-S9, B-9000 Ghent, Belgium
[11] European Space Research and Technology Centre, Keplerlaan 1, 2200 AG Noordwijk, Netherlands
[12] Department of Astronomy, The Oskar Klein Center, Stockholm University, AlbaNova, SE-10691 Stockholm, Sweden
[13] DARK, Niels Bohr Institute, University of Copenhagen, Jagtvej 128, DK-2200 Copenhagen, Denmark
[14] Minnesota Institute for Astrophysics, University of Minnesota, 116 Church Street, S.E., Minneapolis, MN 55455, USA
[15] Finnish Centre for Astronomy with ESO (FINCA), University of Turku, FI-20014 Finland
[16] Tuorla Observatory, Department of Physics and Astronomy, University of Turku, FI-20014 Finland
[17] TMT International Observatory, 100 W. Walnut Street, Pasadena, CA 91124, USA
[18] Department of Physics, KTH Royal Institute of Technology, The Oskar Klein Centre, AlbaNova, SE-106 91 Stockholm, Sweden
[19] Oskar Klein Centre, Department of Astronomy, Stockholm University, Albanova University Centre, SE-106 91 Stockholm, Sweden
[20] Department of Physics and Astronomy, Purdue University, West Lafayette, IN 47907, USA
[21] Steward Observatory, University of Arizona, 933 N. Cherry Avenue, Tucson, AZ 85721, USA
[22] European Southern Observatory, Karl-Schwarzschild-Str 2, Garching D-85748, Germany
[23] Department of Astrophysical Sciences, Princeton University, Princeton, NJ 08544, USA
[24] Texas A&M University, Physics & Astronomy and Mitchell Institute for Fundamental Physics & Astronomy, 4242 TAMU, College Station, TX 77843-4242, USA
[25] Department of Astronomy, University of Texas at Austin, Austin, TX 78712-1205, USA
Received 2023 August 22; revised 2023 September 22; accepted 2023 September 22; published 2023 December 11

Abstract

JWST Near Infrared Camera (NIRCam) observations at 1.5–4.5 μm have provided broadband and narrowband imaging of the evolving remnant of SN 1987A with unparalleled sensitivity and spatial resolution. Comparing with previous marginally spatially resolved Spitzer Infrared Array Camera (IRAC) observations from 2004 to 2019 confirms that the emission arises from the circumstellar equatorial ring (ER), and the current brightness at 3.6 and 4.5 μm was accurately predicted by extrapolation of the declining brightness tracked by IRAC. Despite the regular light curve, the NIRCam observations clearly reveal that much of this emission is from a newly developing outer portion of the ER. Spots in the outer ER tend to lie at position angles in between the well-known ER hotspots. We show that the bulk of the emission in the field can be represented by five standard spectral energy distributions, each with a distinct origin and spatial distribution. This spectral decomposition provides a powerful technique for distinguishing overlapping emission from the circumstellar medium and the supernova ejecta, excited by the forward and reverse shocks, respectively.

Unified Astronomy Thesaurus concepts: Circumstellar dust (236); Core-collapse supernovae (304); Infrared astronomy (786); Large Magellanic Cloud (903); Ring nebulae (1401); Supernova remnants (1667)

Supporting material: animations

1. Introduction

The last 36 yr of observations of SN 1987A have revealed a wealth of information on the evolution, composition, dynamics, and morphology of the supernova (SN) ejecta and its surrounding circumstellar medium (CSM). SN 1987A was observed at almost all wavelengths from gamma-ray to radio, revealing the underlying physical processes of the SN explosion and its aftermath, as reviewed by Arnett et al. (1989), McCray (1993, 2007), and McCray & Fransson (2016). Most relevant to the current analysis are the advances in our understanding of the equatorial ring (ER) around the SN, the origin of its infrared (IR) emission, and the interaction of the ER with the advancing SN blast wave.

SN 1987A is the first SN for which the CSM from the progenitor star can be spatially resolved and the transition from SN to supernova remnant (SNR) can be observed with modern instrumentation. The densest concentration of the CSM was

Original content from this work may be used under the terms of the Creative Commons Attribution 4.0 licence. Any further distribution of this work must maintain attribution to the author(s) and the title of the work, journal citation and DOI.

found to be an ER, rather than a spherical shell. This was first inferred from the presence of narrow UV and optical emission lines from gas that was flash ionized and excited by the UV flash generated by the shock breakout through the surface of the progenitor star (Fransson et al. 1989; Fransson & Lundqvist 1989; Wood et al. 1989; Lundqvist & Fransson 1991; Dwek & Felten 1992). As the glare of the SN faded, the first images of this ring structure were obtained about 3 yr after the explosion (Wampler et al. 1990; Panagia et al. 1991) and two fainter "outer" rings centered north and south of the SN were also revealed.

Measurements of the photoionized ER after the SN explosion indicated a projected semimajor axis of $0\farcs82$ (=0.20 pc = 0.65 ly at a distance of 50 kpc) and an inclination of ~43°, with the north side being nearer (Jakobsen et al. 1991; Panagia et al. 1991; Burrows et al. 1995; Plait et al. 1995). There is evidence that the ER is not quite intrinsically circular, with $b/a = 0.98$ (Sugerman et al. 2005).

Very similar ERs have been seen around some other blue supergiants, with similar structure in the equatorial clumps and mild eccentricity (e.g., Brandner et al. 1997; Smith 2007; Smith et al. 2013). Rings like this might arise at the interaction between a blue supergiant wind and a preceding red supergiant wind (Blondin & Lundqvist 1993; Chevalier & Dwarkadas 1995; Martin & Arnett 1995) or from the ejecta in a stellar merger event (Morris & Podsiadlowski 2009).

The direct interaction of the SN shock with the ER manifested itself in 1995 with the first appearance of bright optical hotspots (or knots) on the northeast quadrant of the ER (Sonneborn et al. 1998; Lawrence et al. 2000). The hotspots are clumps of dense gas that are lit up as the shock propagates into them. With the progression of the shock, more hotspots appeared to fully encircle the ring by 2005 (Fransson et al. 2015; Kangas et al. 2023). About 4 yr later (day ~8000), the total brightness of the ER was fading at most visible wavelengths (Fransson et al. 2015).

The ER was first imaged at the mid-IR wavelength with the Thermal-Region Camera Spectrograph (T-ReCS; Telesco et al. 1998) on the 8.1 m Gemini South Telescope by Bouchet et al. (2004). Photometric light curves at 10 and 20 μm showed that around day 4000 the dominant contribution to the SN energy output transitioned from the ejecta to the shock–ER interaction. The mid-IR emission (3–40 μm) arises from pre-existing ER dust that is collisionally heated by the shocked X-ray-emitting gas.

The Spitzer (Werner et al. 2004; Gehrz et al. 2007) Infrared Spectrograph (IRS; Houck et al. 2004) 5–30 μm spectrum of the ER showed that the emitting dust consists of ~160–180 K silicate grains with radii of $a \gtrsim 0.2$ μm (Bouchet et al. 2006; Dwek et al. 2010). The IRS spectrum also showed an excess of 5–8 μm emission over that of the silicate dust, a spectral component that has been attributed to emission from very small, $a < 0.03$ μm, and hot, $T \sim 350$–500 K, grains with several candidate compositions (Dwek et al. 2010). Assuming that the two dust components reside in the same shocked gas, the small hot grains should have lifetimes that are about 10 times shorter than the larger silicate grains. Jones et al. (2023) use new James Webb Space Telescope (JWST; Gardner et al. 2023) observations to address the issue of small hot grains. Notably, they find that the full mid-IR spectrum can be modeled with a single grain composition, but multiple temperatures are required.

Photometric mid-IR light curves obtained with Spitzer showed a similar evolutionary behavior, manifested by an approximately constant 24–3.6 μm flux ratio up to day ~ 8000, which marked the end of the Spitzer cryogenic era. Subsequent warm-era Spitzer photometric observations showed that the 3.6 and 4.5 μm light curves peaked around day 8000 and started to decline after day ~8500 (Arendt et al. 2016, 2020). This behavior is also exhibited by ground-based J, H, and K_s measurements (Kangas et al. 2023). Arendt et al. (2020) showed that these light curves can be modeled as the product of a convolution of a Gaussian and an exponential function.

The 3.6 and 4.5 μm light curves are generated by the small hot grains. Due to grain sputtering, this emission is expected to drop significantly below the mid-IR light curve when the age of the shocked gas exceeds the lifetime of the small grains, but is still shorter than the lifetime of larger silicate grains (Dwek et al. 1996, 2008). The lack of any mid-IR photometry beyond day 8000 prevented this prediction from being tested with Spitzer, but the JWST Mid Infrared Instrument (MIRI) Medium Resolution Spectrometer (MRS; Wright et al. 2023) observations indicate that the relative brightness of the hot dust has decreased with respect to the cooler dust (Jones et al. 2023).

The high-resolution JWST Near Infrared Camera (NIRCam; Rieke et al. 2023) broadband and narrowband images at 1.5–4.5 μm presented in this paper allow us to address several issues raised by previous observations, namely the consistency between the Spitzer Infrared Array Camera (IRAC) and JWST NIRCam images and photometry, the validity of the light-curve model at later epochs, the origin of the hot emission component, the interaction of the blast wave with the ER, and variations in the spectral energy distribution (SED) of the various spatial components of the ER and the immediate surrounding medium.

We review the JWST NIRCam data and its processing in Section 2. In Section 3, we compare the NIRCam data with the Spitzer IRAC (Fazio et al. 2004) imaging and photometry. The much lower-resolution IRAC images had only hinted at the complex structure of the region. Deconvolution of these images (Arendt et al. 2020) to a $0\farcs2$ resolution suggested that the region is comprised of three stars and the ER, with no noticeable emission from the ejecta at 3.6 and 4.5 μm. The newly obtained high-resolution JWST NIRCam images validate the results of the deconvolution and show that there were no major morphological changes between the Spitzer and JWST eras. The JWST observations enable the use of aperture photometry to obtain a more accurate determination of the brightness of the ER, separate from the confusion of the nearby stars. The NIRCam F356W and F444W photometry is used to extend the 16 yr long light curves measured by Spitzer by another 3 yr.

In Section 4, we take a close look at the extended emission (brightest in the F444W band) beyond the well-known hotspots of the ER. The structure in this new outer ER region is found to be anticorrelated with the ER hotspots, an apparent imprint on the structure of shocks that have swept around and past the hotspots.

In Section 5, we use selected SED templates to decompose the NIRCam images into different spatial structures associated with each of the templates. This technique can separate the structures of overlapping components, and residuals provide indications of where additional or modified components may exist.

Our results are summarized in Section 6.

2. Data

The observations (on day 12,975 since the explosion of SN 1987A; Matsuura et al. 2021) comprise NIRCam images in the wide bands F150W, F200W, F356W, and F444W and the narrow bands F164N, F212N, F323N, and F405N. All the JWST NIRCam data used in this paper can be found at doi:10.17909/dzkq-7c90. The wide bands provide the overall SED of the spatially resolved emission. The selected narrow-band filters are designed to isolate specific spectral lines of H_2 (F212N, F323N), H I (F405N), and a blend of Fe II and Si I (F164N). With JWST, we now have the ability to spatially resolve the locations of these species in great detail.

The images were processed to use improved calibration, astrometry, and subtraction of artifacts and correlated noise with respect to the standard pipeline results (in the MAST archive).[26] We used the world coordinate system alignment tool JHAT (Rest et al. 2023) to align the NIRCam images to Gaia Data Release 2. To remove residual striping, in this work median values per row are subtracted for each detector. To remove the overall background, the median value of each image is subtracted as well. When used for the spectral decomposition (in Section 5), all of the shorter-wavelength images are additionally convolved to the 0.″145 FWHM resolution of the F444W image. See Matsuura et al. (2023a) for further details.

The images are reprojected from their intrinsic orientation and scale to a common grid in (α, δ) coordinates, with the pixel scale of the short-wavelength images. These are shown in Figure 1. Figures 2 and 3 are grayscale and three-color animations of these eight images that provide an alternate way of comparing the brightness, structure, and color of the emission at different wavelengths.

We also show emission-line images in Figure 1, which are constructed by subtracting scaled versions of the corresponding wideband images. In principle, this can remove the continuum contribution in the narrowband images. However, the process is imperfect, because the continuum in the wideband images has variations in color and because the wideband images contain (diluted) contributions from the targeted emission lines as well as other lines within the wider bandwidths.

3. Comparison with Spitzer IRAC

SN 1987A had been monitored at roughly six-month intervals throughout the Spitzer mission in order to trace the evolution of the SN (Bouchet et al. 2006; Dwek et al. 2008, 2010; Arendt et al. 2016, 2020). During Spitzer's cryogenic mission, the observations used all instruments, but after the helium ran out in 2009 May, the observations through 2019 September used only IRAC imaging at 3.6 and 4.5 μm. These bands are very similar to the F356W and F444W bands of NIRCam.

Figure 4 shows a comparison of the 3.6 and 4.5 μm imaging available from IRAC versus that from NIRCam. The IRAC imaging shown here (Arendt et al. 2020) used deconvolution techniques to achieve sufficient resolution to barely resolve the ER. The comparison validates that deconvolution, which showed that the west side of the ER was brighter than the east, and separated out Stars 2, 3, and 4. (Note that the designation of Star 4—"Star A" in Kangas et al. 2023, the brightest one to the southwest (Figure 5)—follows Arendt et al. 2020, and this is not the same as Star 4 of Walker & Suntzeff 1990.)

With normal processing of IRAC data at single epochs, the SN was not resolved from stars 2, 3, and 4. Thus, aperture photometry measured the combined fluxes of the SN and these stars, and estimates of the stellar fluxes based on extrapolation of *JHK* photometry were subtracted to obtain the SN brightness. For comparison with the IRAC measurements, we performed aperture photometry on the NIRCam images using large apertures that replicated those used for IRAC. These apertures and the resulting flux densities are shown in the top row of Figure 5. The second row shows similar integrated photometry from the SN alone, with a smaller aperture that excludes stars 2, 3, and 4. Special masking (indicated in the figure) was applied so that Star 3 did not affect the background measurements. The last row of Figure 5 shows aperture photometry for stars 2, 3, and 4, individually. Star 2 is well represented by a 21,000 K model atmosphere, as is appropriate for an early B-type star. Star 4 appears to be slightly cooler, as might be anticipated by its lower brightness. Star 3 is a known classical Be star (Wang et al. 1992; Walborn et al. 1993) and shows excess emission at $\lambda > 3$ μm, which is typical of these stars. The photometry is listed in Table 1.

Figure 6 compares the modeled (not directly measured) photometry of these stars with IRAC (Arendt et al. 2020) at 3.6 μm with the NIRCam F356W measurement. The results for Stars 2 and 4 indicate that the IRAC and NIRCam results (at 3.6 μm) are consistent and that these stars are stable to within $\sim$10%. Star 3 shows a drop in brightness from IRAC to NIRCam measurements. This may be the intrinsic variability of the Be star, but it is also possible that, being the closest star to the ER, its IRAC flux density estimates were contaminated by emission from the ER. Future NIRCam observations of SN 1987A will definitively reveal the intrinsic variability of Star 3 at the NIRCam wavelengths (see Walborn et al. 1993).

During the Spitzer cryogenic mission, the brightness of SN 1987A had been steadily increasing. Continued monitoring during the warm mission showed the brightness peaking and declining at 3.6 and 4.5 μm. Arendt et al. (2020) found that these light curves could be well modeled as the convolution of a Gaussian function and an exponential decay term. One interpretation of this is that the Gaussian function represents the column density distribution of material swept up in the ER (combined with light travel times from the near to far side of the ER), and the exponential decay represents the temporal evolution of the emissivity of each small parcel of gas and dust, starting from the moment it is shocked. In Figure 7, we show the IRAC light curves and the original models. We have added the new NIRCam measurements and extrapolated the models to the time of the new observations. At both wavelengths, the extrapolations are within a few percent of the NIRCam measurement, indicating that the empirical model continues to serve as a good predictor of the SNR brightness. However, there is some hint of flattening of the 3.6 μm light curve if one compares the final IRAC epochs with the NIRCam measurement. This may reflect unrecognized systematic errors in the late Spitzer 3.6 μm measurements, which are more susceptible to noise and to contamination from Stars 2 and 3 than the 4.5 μm measurements. However, if it is a real trend borne out

[26] https://archive.stsci.edu/

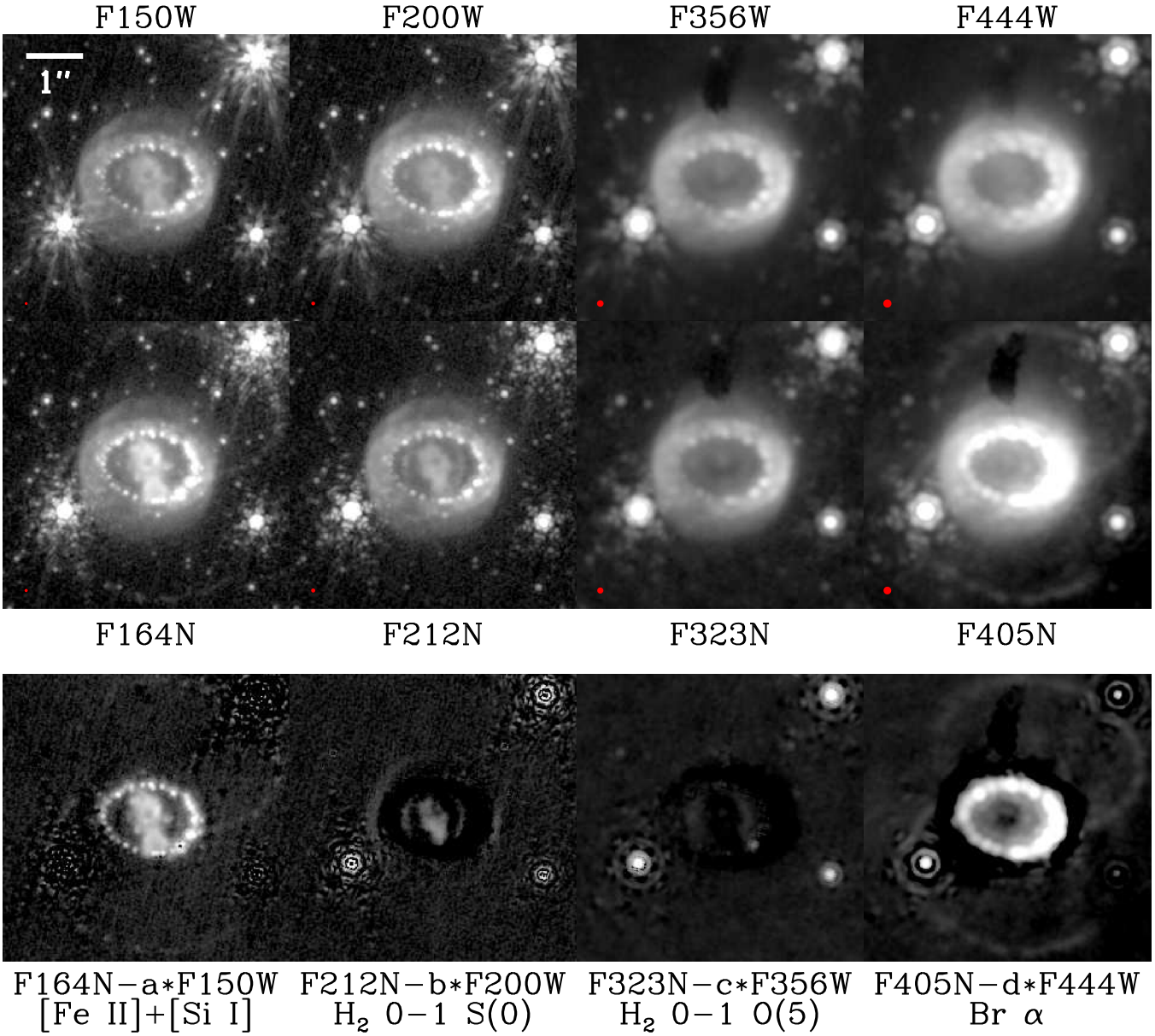

Figure 1. NIRCam images of SN 1987A reprojected onto a common (α, δ) coordinate grid. The top row contains the broadband images. The middle row shows narrowband images that are respectively centered on lines for: [Fe II]+[Si I], H_2, H_2 (also), and H I. The images are logarithmically scaled from 0.32 to 32 MJy sr^{-1} (after adding an offset of 0.5 MJy sr^{-1}) and show a field of view of 5″ × 5″. North is up and east is to the left in all images in this paper. The red dots in the lower left corner of each panel indicate the FWHM size of the PSF. The relative brightness variations between the inner ejecta, the hotspots of the ER, and the emission beyond the ER hotspots indicate a variety of emission mechanisms at work. The bottom row emphasizes the line emission in each of the narrow bands by subtracting scaled versions of the wideband emission.

by future JWST observations, this may reflect the development of the reverse-shock (RS) structure beyond the knotty ER. The brightest location of the RS to the northeast of the ER exhibits a bluer SED than that of the outer ER (see Section 5.1).

4. Structure of the ER

One of the surprises in the NIRCam images is the diffuse outer ER that lies just outside the bright hotspots of the ER at all wavelengths. The structure had not been seen directly in ground-based near-IR imagining prior to 2017, but comparison with Hubble Space Telescope (HST) data suggests that diffuse IR emission began appearing in about 2013 (Kangas et al. 2023). There has been evidence of this structure in HST observations (Fransson et al. 2015; Larsson et al. 2019a), but it is far more prominent in the more recent and longer-wavelength NIRCam data and is clearly traced by He I emission in the RS (Larsson et al. 2023). An interesting detail of this is shown in Figures 8 and 9. The low-contrast spots in the diffuse outer ER are usually found at position angles between the bright hotspots of the inner portion of the ER. This may indicate that the ER hotspots are imprinting small-scale structure on the RS as it is swept out past the ER. Alternatively, it could be an indication of material (dust) from the lower-density portions of the ER (or ablated from the hotspots) that has been entrained in the blast wave that propagated between and around the denser hotspots of the ER. This is supported by the fact that the mid-IR (silicate) emission is now spatially resolved by both the ground-based and JWST MIRI imaging and is found to lie in this diffuse region exterior to the bright

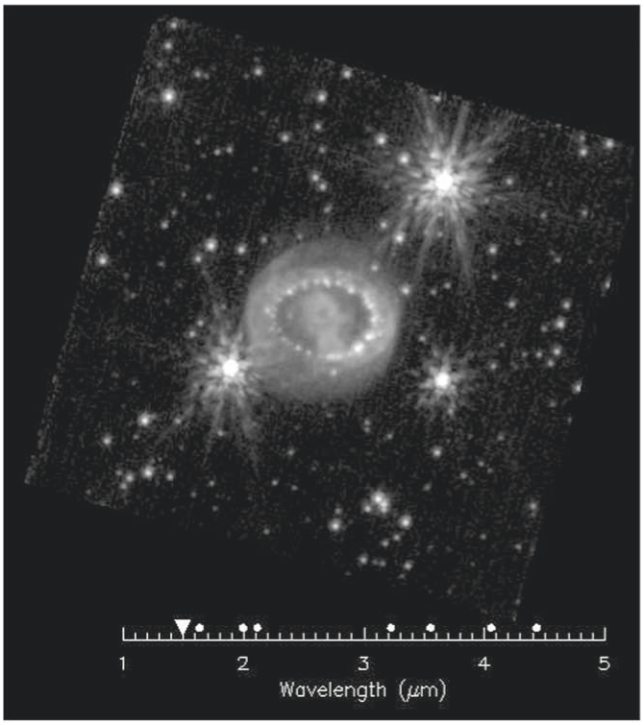

Figure 2. Animated comparison of the SN 1987A emission in the different NIRCam bands. Showing the data of Figure 1 as a single image while smoothly transitioning between wavelengths reveals similarities and differences between the structures at different wavelengths. As the 18 s animation plays, the scale bar and pointer at the bottom indicate which wavelength, or intermediate blend of wavelengths, is displayed.

(An animation of this figure is available.)

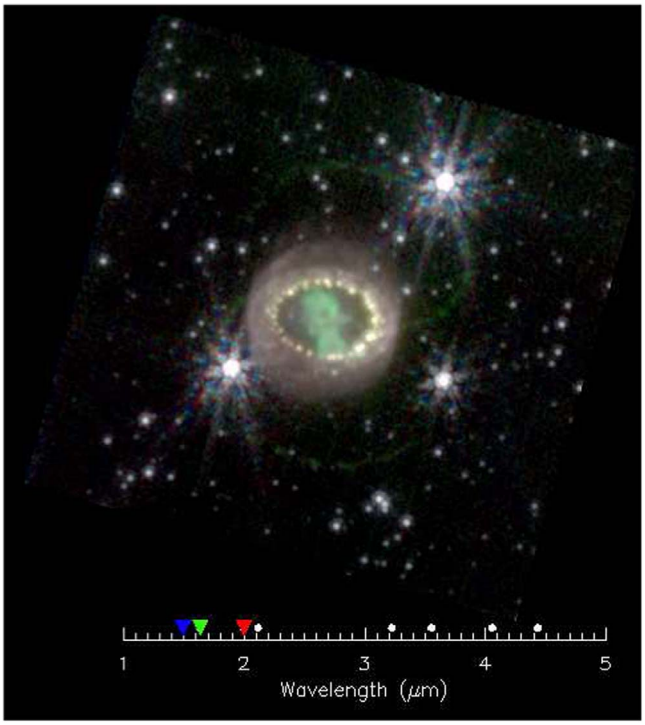

Figure 3. Animated three-color comparison of the SN 1987A emission in the different NIRCam bands. Similar to Figure 2, this animation helps highlight color differences between different structures. As the 13 s animation plays, the scale bar and pointers at the bottom indicate which wavelength, or intermediate blend of wavelengths, is displayed in each of the red, green, and blue channels.

(An animation of this figure is available.)

ER hotspots (Matsuura et al. 2022; P. Bouchet et al. 2023 in preparation; Jones et al. 2023). It will be interesting to check the proper motion of these features relative to the bright hotspots with future observations.

An outer emission component on the west side of the ER has previously been observed with HST in the F502N [O III]-dominated filter, suggested to originate from gas swept up by the blast wave propagating in the low-density medium between the hotspots (Larsson et al. 2019a). In addition, the HST images reveal faint outer spots (mainly in the southeast) and diffuse emission in Hα, which likely originate from high-latitude material. The high-latitude emission from the RS was noted by HST in Lyα and Hα (Michael et al. 2003; France et al. 2015), as well as from radio emission (Ng et al. 2008; Fransson et al. 2013; Larsson et al. 2019a).

5. Spectral Decomposition

The distinct structures and their colors that are evident in the NIRCam images (see Matsuura et al. 2023a and Figure 1) suggest that it may be useful to decompose the spatial structure of the images into separate components, each characterized by a different spectrum. Such a decomposition can reveal the spatial locations of various emission mechanisms and physical conditions, even in places where multiple components overlap. This form of spectral decomposition has previously been applied to the Cas A SNR (Arendt et al. 2014).

To perform the spectral decomposition, at each point (coordinates (α, δ)) in the images the observed SED, $I_\nu(\alpha, \delta)$,

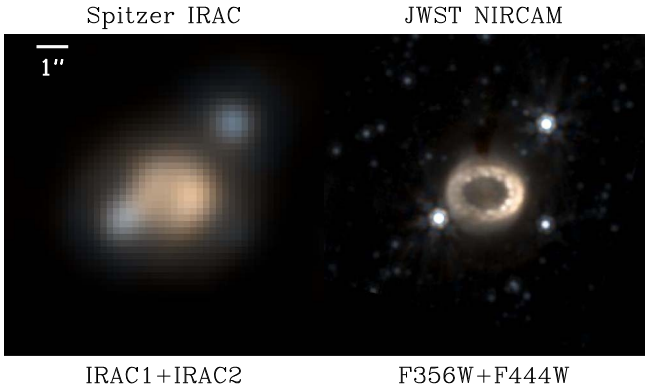

Figure 4. Comparison of IRAC and NIRCam images at comparable wavelengths provides a qualitative indication that the high-resolution mapping and deconvolution of the IRAC data (Arendt et al. 2020) had revealed hints of the true structure of the SNR emission, and that there have been no major changes between the Spitzer and JWST eras.

is modeled as the sum of several template SEDs, $F_{\nu,i}$, representing different emission sources or mechanisms:

$$I_\nu(\alpha, \delta) = \sum_i A_i(\alpha, \delta) F_{\nu,i}, \quad (1)$$

where $A_i(\alpha, \delta)$ are the coefficients to be determined at each location. With eight bands, we can solve for no more than eight free parameters at each location, i.e., no more than eight spectral components. In the analysis below, we investigate two alternative choices of five SED templates, $F_{\nu,i}$ for $i = 1,5$. The parameters $A_i(\alpha, \delta)$ are determined though χ^2 minimization.

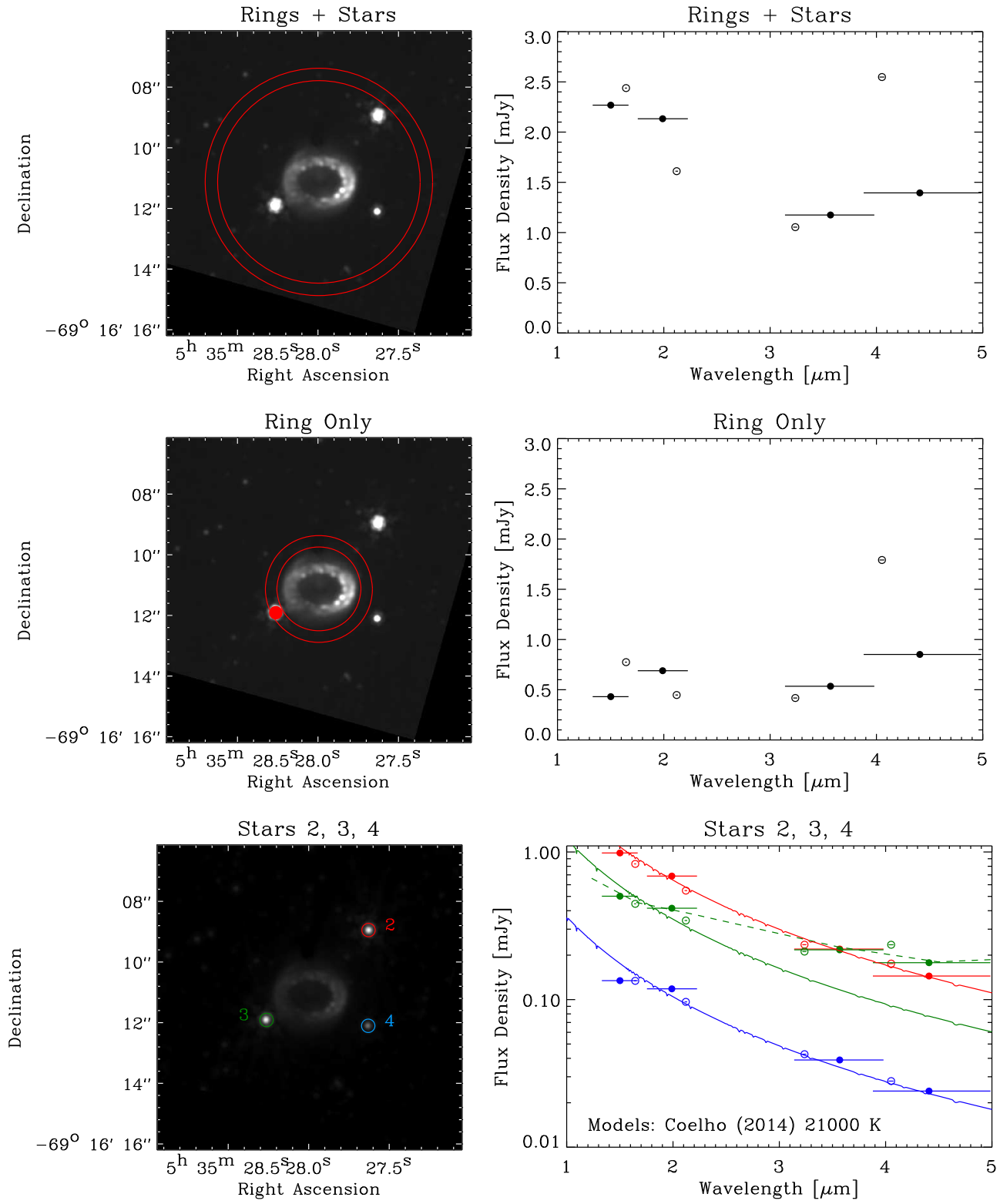

Figure 5. The top row shows (left) apertures used to replicate the IRAC photometry that had been performed on much lower-resolution data, and (right) the resulting SED. These flux densities are the sum of those for the SN and stars 2, 3, and 4. The horizontal lines indicate the bandwidths for wide bands (filled circles) and narrow bands (open circles). The middle row shows results with a smaller aperture that includes only the SN. Star 3 is specifically excluded from the background region. The bottom row shows the SEDs of stars 2, 3, and 4, with 21,000 K stellar atmosphere models from Coelho (2014) shown for comparison. Star 3 is a classical Be star with excess emission at >3 μm. The green dashed line shows the SED of the B2IIIe star SMC5_074402 from Bonanos et al. (2010) for comparison (multiplied by a factor of 0.8). The display range on the bottom left panel is altered such that the stars are not saturated.

However, the χ^2 values do not capture the degree to which the $A_i(\alpha, \delta)$ parameters are spatially distinct from one another, and nonnegative, which are both important considerations here.

We had also applied principal component analysis to the NIRCam data. This does not yield components that are easier to interpret than the original images, but it does indicate that at

Table 1
Flux Densities

Filter	Star 2	Star 3	Star 4	SN 1987A Small Ap.	SN 1987A Large Ap.
F150W	0.985 ± 0.001	0.502 ± 0.001	0.134 ± 0.001	0.431 ± 0.001	2.268 ± 0.001
F164N	0.830 ± 0.001	0.445 ± 0.001	0.134 ± 0.001	0.775 ± 0.001	2.438 ± 0.001
F200W	0.687 ± 0.001	0.416 ± 0.001	0.118 ± 0.001	0.689 ± 0.001	2.133 ± 0.001
F212N	0.548 ± 0.001	0.343 ± 0.001	0.097 ± 0.001	0.447 ± 0.001	1.611 ± 0.001
F323N	0.235 ± 0.001	0.212 ± 0.001	0.043 ± 0.001	0.418 ± 0.001	1.054 ± 0.001
F356W	0.220 ± 0.001	0.217 ± 0.001	0.039 ± 0.001	0.535 ± 0.001	1.175 ± 0.001
F405N	0.175 ± 0.001	0.235 ± 0.001	0.028 ± 0.001	1.792 ± 0.003	2.548 ± 0.002
F444W	0.144 ± 0.001	0.178 ± 0.001	0.024 ± 0.001	0.851 ± 0.002	1.395 ± 0.001

Note. Units = mJy.

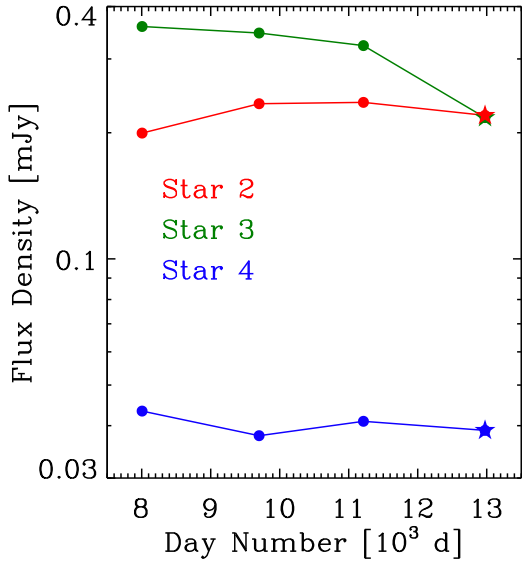

Figure 6. 3.6 μm stellar photometry (light curves) of stars 2, 3, and 4. The filled circles are modeled brightnesses from IRAC data (Arendt et al. 2020), where the stars are not fully resolved. The filled star symbols at day 12,975 indicate NIRCam measurements. Stars 2 and 4 appear to be stable, while Star 3 (a classical Be star) appears to show a decreased brightness. Star 3 is intrinsically variable, but, in addition, the IRAC flux densities may have been affected by confusion with the ER.

least five spectral components are warranted when modeling the emission in the data set.

5.1. Decomposition with Sampled SEDs

For this decomposition, we chose five spectral templates that are selected from the observed SEDs at representative locations around SN 1987A, as shown in Figure 10.

1. $F_{\nu,1}$ is the mean SED of Stars 2 and 4, chosen to represent stellar emission around the field.
2. $F_{\nu,2}$ is the SED of the brightest portion of the smooth outer part of the ER, chosen to represent this newer development of the ER structure.
3. $F_{\nu,3}$ is the SED of a bright ER hotspot, representing the older and more prominent structure of the ER.
4. $F_{\nu,4}$ is an SED in the northern lobe of the inner ejecta, representative of this component.
5. $F_{\nu,5}$ is the SED at a diffuse arc of emission to the northeast of the ER, which represents the developing RS in regions beyond the ER.

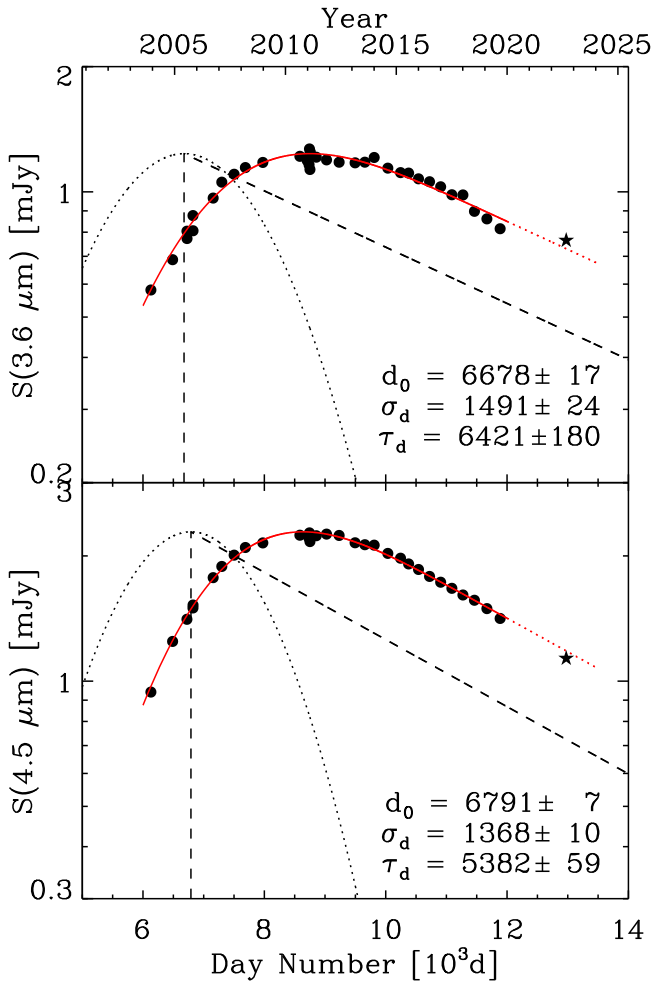

Figure 7. The IRAC light curves at 3.6 and 4.5 μm are shown with filled circles. The NIRCam measurements are indicated with filled stars at day 12,975. Formal random uncertainties are smaller than the plotted symbols. For consistency with the IRAC measurements, these are the large-aperture flux densities minus 0.41 and 0.26 mJy estimates for the 3.6 and 4.5 μm combined brightness of Stars 2 and 3. The dashed red line shows that an extrapolation of the IRAC model (solid red line; Arendt et al. 2020) is a good predictor of the NIRCam flux densities. The IRAC models are the convolution of a Gaussian function and an exponential function (shown as black curves at d_0).

The SEDs of the stars and the outer ER seem to be dominated by continuum emission. The ER hotspot and the ejecta SEDs have strong line emission components, as evidenced by their prominence in the F405N and F164N bands. These characteristics are confirmed (at lower spatial

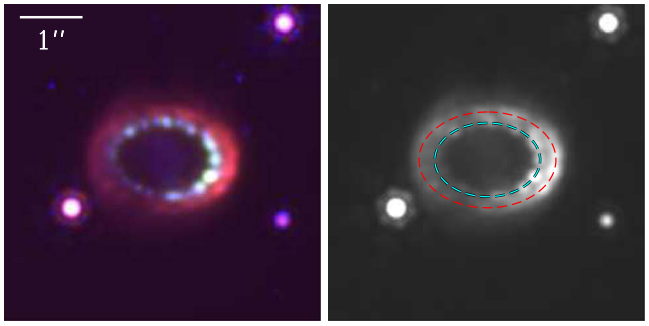

Figure 8. Locations of ER hotspots and clumps. Left: images at F444W (red), F405N (green), and F200W (blue). Right: F444W image superimposed with ellipses tracing the bright hotspots (blue) and the outer emission (red) as shown in Figure 9.

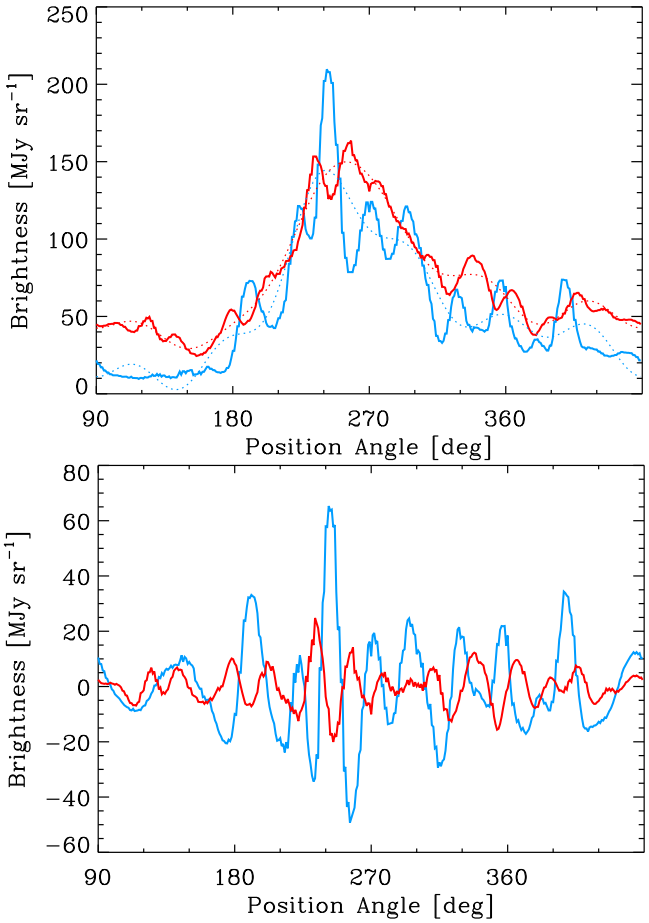

Figure 9. Correlation of the brightness in the inner ER (at F405N) and the outer ER (at F444W). Top: brightness as a function of deprojected position angle along the Figure 8 ellipses tracing the bright hotspots (blue) and the outer emission (red, multiplied by 5). Position angle is measured eastward from north along the ring as if it were viewed face on. The dotted lines show the large-scale variation as traced by the lowest-frequency components of the Fourier transform. Bottom: the small-scale structure of the bright hotspots (blue) and outer emission (red, multiplied by 5) after subtraction of the large-scale background indicated in the top panel. The spots in the outer portion of the ER are anticorrelated in position angle with the bright hotspots with a correlation coefficient of −0.38.

resolution) by the NIRSpec observations of Larsson et al. (2023). The ∼3400 km s^{-1} FWHM of the NIRCam narrow-band filters should be sufficient to capture the bulk of the line emission from the ER and the inner ejecta. Line emission in the RS can appear at velocities up to ∼10,000 km s^{-1} (e.g.,

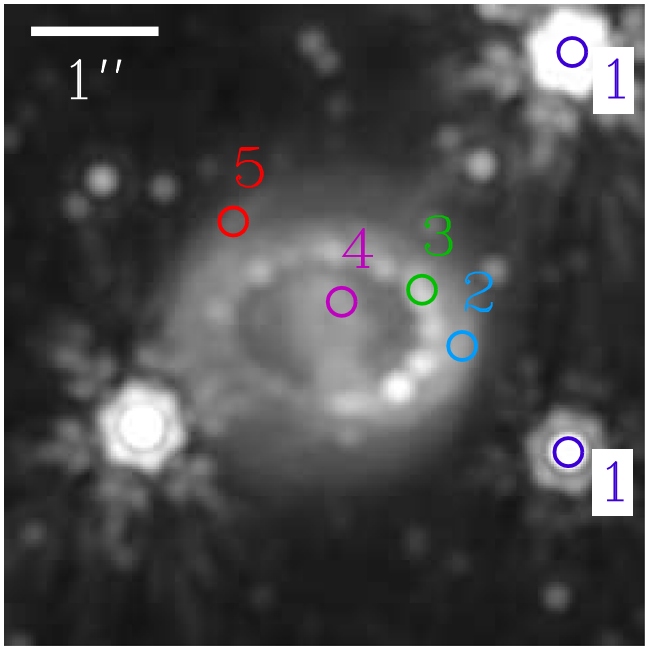

Figure 10. Locations chosen for the empirical SEDs used for spectral decomposition, indicated on the F150W image after convolution to F444W resolution. See Section 5.1. The crop and display range are the same as Figure 1.

Michael et al. 1998; Sonneborn et al. 1998; Smith et al. 2005; France et al. 2010; Fransson et al. 2013; Larsson et al. 2019a), but comparison of the NIRCam narrowband images with the corresponding wideband images does not indicate the presence of significant line emission in the wide bands that is missed by the narrow bands due to velocity shifts. In these NIRCam data, the RS appears to be dominated by continuum emission.

Figure 11 shows the five template SEDs and the derived spatial distributions of each. (Imperfections in convolving to a common resolution leaves ring-like artifacts around bright stars and hotspots. These should be disregarded.) The emission of stars is largely captured by the first template (the SED of Stars 2 and 4). Note that this template clearly picks out the faint star that is superimposed on the southwest part of the ER.

The outer ER SED component shows a strong gradient (about a factor of 5) in brightness across the ER. This component also seems to trace the outer portions of the inner ejecta, which suggest that there are spatial variations in the SED of the inner ejecta. This may arise from asymmetry in the radiation field of the ER and RS, which heats the inner ejecta, with possible contribution from variations of the composition or density of the inner ejecta.

Emission from the ER hotspot SED captures the other hotspots around the inner ER, which are notably weak in the southeast portion of the ER. This component also accounts for much fainter emission from the outer rings of the pre-SN CSM.

The inner ejecta SED clearly defines the spatial distribution of this component, apparently even in the south, where it is beginning to overlap with the ER. The $A_i(\alpha, \delta)$ for the inner ejecta has moderate negative values outlining bright hotspots in the ER. This may indicate that the ER hotspot SED is not exactly appropriate, due to changes in the emission between the cores and periphery of the ER hotspots, or it may be a result of imperfect point-spread function (PSF) matching, as with the artifacts around stars.

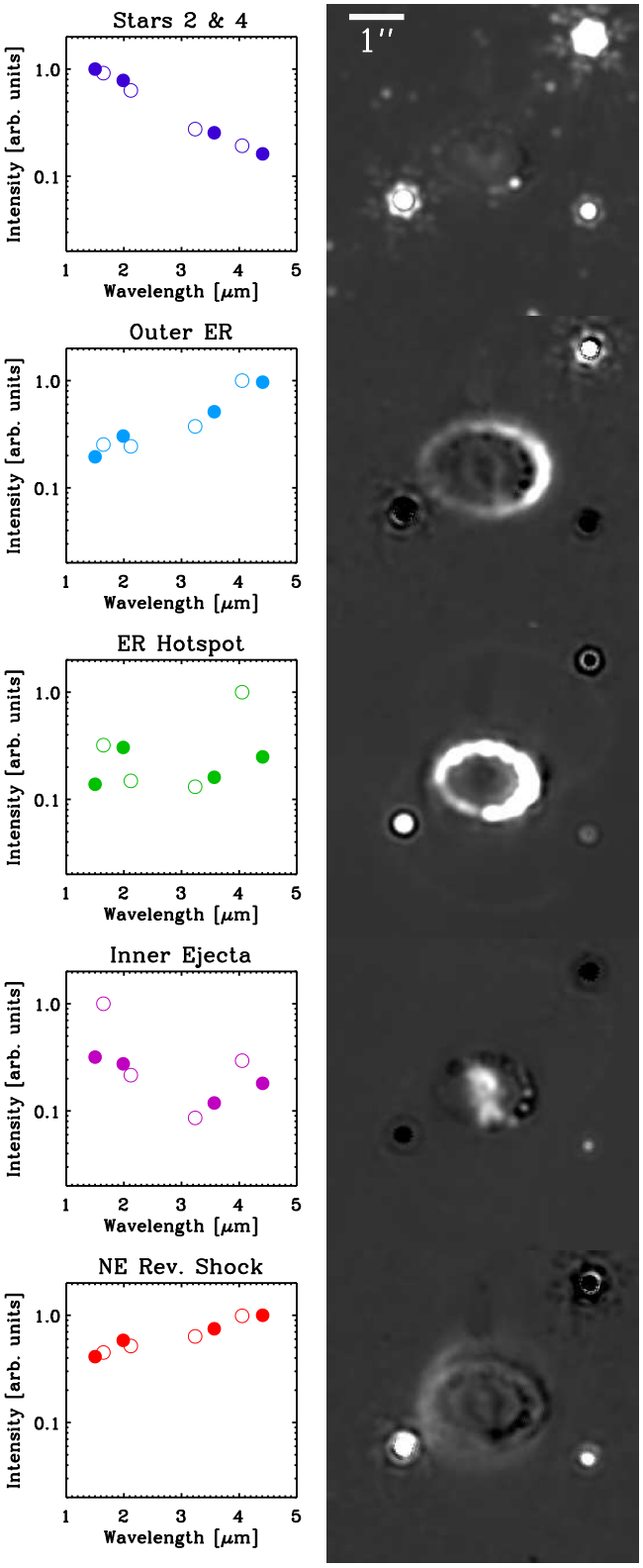

Figure 11. Spectral decomposition using observed SEDs. The SEDs, $F_{\nu,i}$, (from locations shown in Figure 10) are shown in the left column. Wide filter bands are indicated with filled circles, narrow ones with open circles. The figures in the right column show the derived spatial distribution of the emission, $A_i(\alpha, \delta)$, from each of the SEDs. All are displayed on the same linear scale [−5, 20] to illustrate the relative importance of the different components.

The appearance of the northeast RS component is somewhat similar to that of the He I 1.083 μm emission that is used to reveal the 3D structure of the RS (Figure 7 of Larsson et al. 2023). (This structure is also traced in Hα; Larsson et al. 2019a.) However, in He I, the emission seems brightest in the northeast and southwest. Here, there seems to be an east–west gradient that goes in the opposite direction as the brightness of the outer ER and the dust temperature gradient traced at mid-IR wavelengths in the outer ER (Matsuura et al. 2022; P. Bouchet et al. 2023, in preparation; Jones et al. 2023). On the west side, negative spots are found in the northeast RS component at bright ER hotspots and bright regions of the outer ER, although the structure seems heavily influenced by small resolution mismatches. However, the resulting $A_i(\alpha, \delta)$ image does not match well with the 315 GHz synchrotron emission mapped by the Atacama Large Millimeter/submillimeter Array (Cigan et al. 2019), despite the fact that the northeast RS does have a spectral index very similar to the radio synchrotron emission. The map of the 315 GHz emission is best correlated with the outer ER, which has a much steeper spectrum in the F356W and F444W bands (see below).

5.2. Decomposition with Physical Spectra

An alternative spectral decomposition is based on SEDs that are expected for different emission mechanisms. We again choose five SED templates.

1. $F_{\nu,1}$ is derived from a 21,000 K blackbody spectrum and is intended to represent stars in the field, especially Stars 2, 3, and 4.
2. $F_{\nu,2}$ is a power-law spectrum with a steep spectral index of $\alpha = -3.0$ that is motivated by the general appearance of the spectrum at ∼3–10 μm (Dwek et al. 2010; Jones et al. 2023) and the specific ratio of F444W and F356W emission on the west side of the outer ER. The east side has a flatter spectral index (Matsuura et al. 2023a). This component represents a combination of continuum emission mechanisms, including thermal emission from dust and synchrotron emission (Jones et al. 2023). The F444W and F356W emissions could alternatively be fit with a blackbody spectrum with $T \approx 580$ K. The blackbody and power law differ by <10% at 3–5 μm, but the blackbody drops much more sharply at shorter wavelengths. Neither a power law nor a blackbody would account for the bound–free continuum that becomes dominant at $\lambda \lesssim 3$ μm (Jones et al. 2023; Larsson et al. 2023).
3. $F_{\nu,3}$ is based on integrating a SINgle Faint Object Near-IR Investigation (SINFONI; Thatte et al. 1998) line emission spectrum of the ER (data from Larsson et al. 2016) across the short-wavelength NIRCam filter bands, and adding Br α emission to the F405N and F444W bands, assuming a line flux ∼0.25 times that measured in the F200W band (Pa α + Br γ).
4. $F_{\nu,4}$ is a similar integration over a SINFONI line emission spectrum of the ejecta (Larsson et al. 2016). In this case, no additional lines are included.
5. $F_{\nu,5}$ is intended to represent H_2 emission (as seen in Fransson et al. 2016; Larsson et al. 2019b, 2023). The model intensities are calculated by integrating the Draine & Bertoldi (1996) `Qm3o` photodissociation region model, as matched to the NIRSpec data (Larsson et al. 2023), over the NIRCam system responses. This component may be particularly relevant, because the F212N and F323N bands target H_2 lines. In the NIRSpec ejecta spectrum, the 3.23 μm line is much weaker than the 2.12 μm line (Larsson et al. 2023).

Figure 12 shows these five template SEDs and the derived spatial distributions of each. The residuals of the fits are somewhat (∼3 times) worse than those of the sampled SEDs from Section 5.1, but the main results are similar, with the following exceptions. The power-law spectrum accounts for both the outer ER and the RS regions beyond, which had similar sampled SEDs. However since the power-law spectrum is relatively weak at short wavelengths, the stellar SED is invoked to provide the short-wavelength continuum (mostly bound–free emission) in these regions (especially in the slightly bluer regions of the RS, e.g., outside the ER to the northeast). If a 580 K blackbody is substituted for the power-law spectrum, then this component is similar, except for no longer tracing the hotspots in the ER, which are instead modeled with increased contributions from the bluer 20,000 K and ejecta components. The H_2 component does isolate the emission of H_2 in the ejecta. This also picks out faint "crescents" between the inner ejecta and the ER, which are the subject of M. Matsuura et al. (2023b, in preparation). However it is relatively weak and also acts as a positive or negative correction term to the other templates.

We also examined this decomposition using the NIRSpec ER and ejecta spectra from Larsson et al. (2023). While these data have complete coverage of the NIRCam bands, and better sensitivity than the SINFONI data, they are less suitable for this analysis because the published spectra are integrated over large regions, where multiple emission components overlap. The ER spectrum, for example, includes the bright hotspots as well as the diffuse outer ER and regions of the RS. Extracting spectra at more localized regions that are dominated by specific emission components leads to better SEDs for use in the spectral decomposition of the NIRCam data.

6. Summary

We have used the high-sensitivity and high-spatial-resolution JWST NIRCam 1.5–4.5 μm imaging to show consistency with the marginally resolved Spitzer IRAC images. We confirmed that the Spitzer 3.6 and 4.5 μm emission arises from the ER, and showed that integrated NIRCam flux densities from the ER in the 3.6 and 4.5 μm bands fall on the predicted extrapolations of the Spitzer 3.6 and 4.5 μm light curves. The extrapolations employ a model in which the light curves are fitted by a convolution of a Gaussian with a decreasing exponential function. The two components may represent the convolution of a (Gaussian) physical distribution of swept-up dust with a sharp onset and exponential decay in the emissivity of the dust, or, conversely, an exponentially declining spatial distribution of dust with a rising and falling (near-Gaussian in shape) emissivity in response to the passing shock. Such mathematical presentation of the evolution of the light curves may not be unique, but the predictive power of the present one remains compelling.

The F356W flux densities of the companion stars are similar to those modeled from the lower-resolution Spitzer images. However, we have not applied the newly measured F356W and F444W flux densities retroactively to the Spitzer data, because the differences from the previously assumed values are relatively small, and because the potential variability of Star 3 adds a similar level of uncertainty.

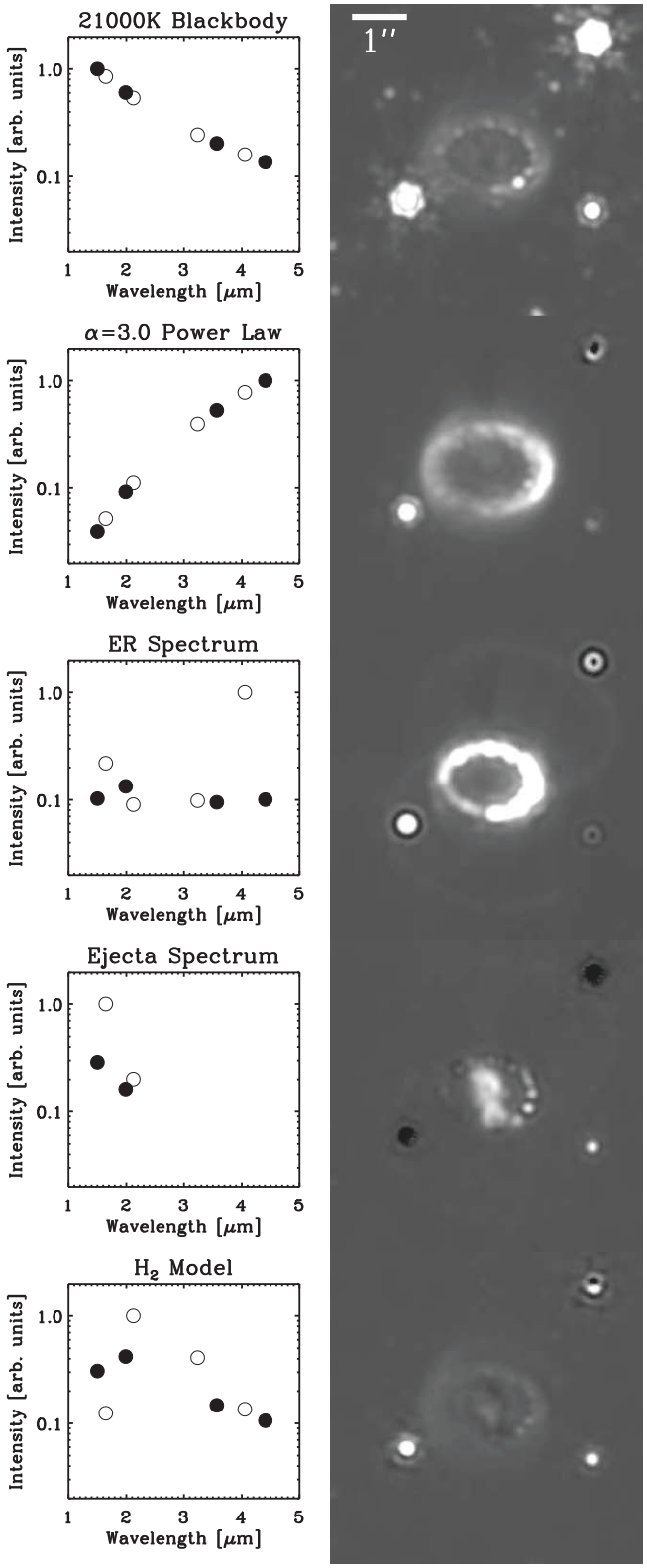

Figure 12. Spectral decomposition using physically motivated SEDs. The SEDs, $F_{\nu,i}$, are shown in the left column. Wide filter bands are indicated with filled circles, narrow ones with open circles. The ejecta spectrum SEDs does not have significant emission in all eight bands. The figures in the right column show the derived spatial distribution of the emission, $A_i(\alpha, \delta)$, from each of the SEDs. All are displayed on the same linear scale [−5, 20] to illustrate the relative importance of the different components.

The NIRCam images allow a detailed analysis of the spatial correlation between the ER hotspots and the diffuse extended emission outside the ER. We find an anticorrelation between the azimuthal distribution of the bright inner hotspots and clumps in the outer diffuse emission. The hotspots seem to leave an imprint on the diffuse emission. One possibility is that the diffuse emission represents the forward shock draping around and extending beyond the hotspots (e.g., Silvia et al. 2010, 2012; Kirchschlager et al. 2019, 2023). The diffuse outer ER seems to coincide with the region where the dominant 10–30 μm emission from silicate dust arises (P. Bouchet et al. 2023, in preparation; Jones et al. 2023).

We used the high-spatial-resolution images of the SN and the companion stars to decompose and represent the emission by two sets of five standard SEDs. One set of these SEDs is chosen from five distinct representative locations in the images. The other set of SEDs is derived from theoretical (blackbody, synchrotron, and H_2) and empirical (ER and ejecta) spectra. These decompositions show that the bulk of the emission can be attributed to only four spectrally and spatially distinct components of the SN (plus a fifth stellar component): the bright inner ER hotspots, the redder and more diffuse outer ER, the inner ejecta, and the RS. The slightly incomplete spatial separation of the components indicates that the inner ejecta shows the most evidence of distinct spatial variations in its SED.

Our analysis of the high-resolution NIRCam SN 1987A images provides a powerful method for dissecting the various components of this extremely young SNR. It separates CSM features excited by the passage of the forward shock, the outer ejecta of the SN passing through the RS, and the metal-rich inner ejecta that is only starting to reach the RS. The future combination of the NIRCam imaging with data from Hubble (with comparable angular resolution) will allow the distinction of spectral variations within these components and/or additional components. The spectral decomposition applied to the JWST NIRSpec and MIRI MRS data cubes (Jones et al. 2023; Larsson et al. 2023) can provide much better definition of the spectral properties of each component, despite the poorer spatial resolution of those data.

Acknowledgments

This work is based on observations made with the NASA/ESA/CSA James Webb Space Telescope. The data were obtained from the Mikulski Archive for Space Telescopes at the Space Telescope Science Institute, which is operated by the Association of Universities for Research in Astronomy, Inc., under NASA contract NAS 5-03127 for JWST. These observations are associated with program #1726. Support for program #1726 was provided by NASA through a grant from the Space Telescope Science Institute, which is operated by the Association of Universities for Research in Astronomy, Inc., under NASA contract NAS 5-03127. Work by R.G.A. was supported by NASA under award No. 80GSFC21M0002. I.D. L. and F.K. acknowledge funding from the European Research Council (ERC) under the European Union's Horizon 2020 research and innovation program (#851622 DustOrigin). C.G. is supported by a VILLUM FONDEN Villum Young Investigator grant (25501). R.D.G. was supported, in part, by the United States Air Force. P.L. thanks the Swedish Research Council for support. M.M. and R.W. acknowledge support from an STFC Consolidated grant (2422911). J.C.W. is supported by NSF grant AST 1813825. We thank the anonymous referee for helpful advice on improvements to the text and figures.

Facility: JWST (NIRCam).

Software: IDLASTRO (Landsman 1995), JHAT (Rest et al. 2023).

ORCID iDs

Richard G. Arendt https://orcid.org/0000-0001-8403-8548
Martha L. Boyer https://orcid.org/0000-0003-4850-9589
Eli Dwek https://orcid.org/0000-0001-8033-1181
Mikako Matsuura https://orcid.org/0000-0002-5529-5593
Aravind P. Ravi https://orcid.org/0000-0002-7352-7845
Armin Rest https://orcid.org/0000-0002-4410-5387
Roger Chevalier https://orcid.org/0000-0002-9117-7244
Phil Cigan https://orcid.org/0000-0002-8736-2463
Ilse De Looze https://orcid.org/0000-0001-9419-6355
Guido De Marchi https://orcid.org/0000-0001-7906-3829
Claes Fransson https://orcid.org/0000-0001-8532-3594
Christa Gall https://orcid.org/0000-0002-8526-3963
R. D. Gehrz https://orcid.org/0000-0003-1319-4089
Haley L. Gomez https://orcid.org/0000-0003-3398-0052
Tuomas Kangas https://orcid.org/0000-0002-5477-0217
Florian Kirchschlager https://orcid.org/0000-0002-3036-0184
Robert P. Kirshner https://orcid.org/0000-0002-1966-3942
Josefin Larsson https://orcid.org/0000-0003-0065-2933
Peter Lundqvist https://orcid.org/0000-0002-3664-8082
Dan Milisavljevic https://orcid.org/0000-0002-0763-3885
Sangwook Park https://orcid.org/0000-0003-3900-7739
Nathan Smith https://orcid.org/0000-0001-5510-2424
Jason Spyromilio https://orcid.org/0000-0001-6815-4055
Tea Temim https://orcid.org/0000-0001-7380-3144
Lifan Wang https://orcid.org/0000-0001-7092-9374
J. Craig Wheeler https://orcid.org/0000-0003-1349-6538
Charles E. Woodward https://orcid.org/0000-0001-6567-627X

References

Arendt, R. G., Dwek, E., Bouchet, P., et al. 2016, AJ, 151, 62
Arendt, R. G., Dwek, E., Bouchet, P., et al. 2020, ApJ, 890, 2
Arendt, R. G., Dwek, E., Kober, G., Rho, J., & Hwang, U. 2014, ApJ, 786, 55
Arnett, W. D., Bahcall, J. N., Kirshner, R. P., & Woosley, S. E. 1989, ARA&A, 27, 629
Blondin, J. M., & Lundqvist, P. 1993, ApJ, 405, 337
Bonanos, A. Z., Lennon, D. J., Köhlinger, F., et al. 2010, AJ, 140, 416
Bouchet, P., De Buizer, J. M., Suntzeff, N. B., et al. 2004, ApJ, 611, 394
Bouchet, P., Dwek, E., Danziger, J., et al. 2006, ApJ, 650, 212
Brandner, W., Chu, Y.-H., Eisenhauer, F., Grebel, E. K., & Points, S. D. 1997, ApJL, 489, L153
Burrows, C. J., Krist, J., Hester, J. J., et al. 1995, ApJ, 452, 680
Chevalier, R. A., & Dwarkadas, V. V. 1995, ApJL, 452, L45
Cigan, P., Matsuura, M., Gomez, H. L., et al. 2019, ApJ, 886, 51
Coelho, P. R. T. 2014, MNRAS, 440, 1027
Draine, B. T., & Bertoldi, F. 1996, ApJ, 468, 269
Dwek, E., Arendt, R. G., Bouchet, P., et al. 2008, ApJ, 676, 1029
Dwek, E., Arendt, R. G., Bouchet, P., et al. 2010, ApJ, 722, 425
Dwek, E., & Felten, J. E. 1992, ApJ, 387, 551
Dwek, E., Foster, S. M., & Vancura, O. 1996, ApJ, 457, 244
Fazio, G. G., Hora, J. L., Allen, L. E., et al. 2004, ApJS, 154, 10
France, K., McCray, R., Fransson, C., et al. 2015, ApJL, 801, L16
France, K., McCray, R., Heng, K., et al. 2010, Sci, 329, 1624
Fransson, C., Cassatella, A., Gilmozzi, R., et al. 1989, ApJ, 336, 429
Fransson, C., Larsson, J., Migotto, K., et al. 2015, ApJL, 806, L19
Fransson, C., Larsson, J., Spyromilio, J., et al. 2013, ApJ, 768, 88
Fransson, C., Larsson, J., Spyromilio, J., et al. 2016, ApJL, 821, L5

Fransson, C., & Lundqvist, P. 1989, ApJL, 341, L59
Gardner, J. P., Mather, J. C., Abbott, R., et al. 2023, PASP, 135, 068001
Gehrz, R. D., Roellig, T. L., Werner, M. W., et al. 2007, RScI, 78, 011302
Houck, J. R., Roellig, T. L., van Cleve, J., et al. 2004, ApJS, 154, 18
Jakobsen, P., Albrecht, R., Barbieri, C., et al. 1991, ApJL, 369, L63
Jones, O. C., Kavanagh, P. J., Barlow, M. J., et al. 2023, ApJ, 958, 95
Kangas, T., Ahola, A., Fransson, C., et al. 2023, A&A, 675, A166
Kirchschlager, F., Schmidt, F. D., Barlow, M. J., et al. 2019, MNRAS, 489, 4465
Kirchschlager, F., Schmidt, F. D., Barlow, M. J., De Looze, I., & Sartorio, N. S. 2023, MNRAS, 520, 5042
Landsman, W. B. 1995, in ASP Conf. Ser. 77, Astronomical Data Analysis Software and Systems IV, ed. R. A. Shaw, H. E. Payne, & J. J. E. Hayes (San Francisco, CA: ASP), 437, J. J. E.
Larsson, J., Fransson, C., Alp, D., et al. 2019a, ApJ, 886, 147
Larsson, J., Fransson, C., Sargent, B., et al. 2023, ApJL, 949, L27
Larsson, J., Fransson, C., Spyromilio, J., et al. 2016, ApJ, 833, 147
Larsson, J., Spyromilio, J., Fransson, C., et al. 2019b, ApJ, 873, 15
Lawrence, S. S., Sugerman, B. E., Bouchet, P., et al. 2000, ApJL, 537, L123
Lundqvist, P., & Fransson, C. 1991, ApJ, 380, 575
Martin, C. L., & Arnett, D. 1995, ApJ, 447, 378
Matsuura, M., Arendt, R., & Dwek, E. 2021, Shocks and expanding ejecta in Supernova 1987A JWST Proposal, Space Telescope Science Institute, 1726
Matsuura, M., Boyer, M., Arendt, R. G., et al. 2023a, MNRAS, submitted
Matsuura, M., Wesson, R., Arendt, R. G., et al. 2022, MNRAS, 517, 4327
McCray, R. 1993, ARA&A, 31, 175
McCray, R. 2007, in AIP Conf. Proc. 937, Supernova 1987A: 20 Years After: Supernovae and Gamma-Ray Bursters, ed. S. Immler, K. Weiler, & R. McCray (Melville, NY: AIP), 3
McCray, R., & Fransson, C. 2016, ARA&A, 54, 19
Michael, E., McCray, R., Chevalier, R., et al. 2003, ApJ, 593, 809
Michael, E., McCray, R., Pun, C. S. J., et al. 1998, ApJL, 509, L117
Morris, T., & Podsiadlowski, P. 2009, MNRAS, 399, 515
Ng, C. Y., Gaensler, B. M., Staveley-Smith, L., et al. 2008, ApJ, 684, 481
Panagia, N., Gilmozzi, R., Macchetto, F., Adorf, H. M., & Kirshner, R. P. 1991, ApJL, 380, L23
Plait, P. C., Lundqvist, P., Chevalier, R. A., & Kirshner, R. P. 1995, ApJ, 439, 730
Rest, A., Pierel, J., Correnti, M., et al. 2023, arminrest/jhat: The JWST HST Alignment Tool (JHAT), v2, Zenodo, doi:10.5281/zenodo.7892935
Rieke, M. J., Kelly, D. M., Misselt, K., et al. 2023, PASP, 135, 028001
Silvia, D. W., Smith, B. D., & Shull, J. M. 2010, ApJ, 715, 1575
Silvia, D. W., Smith, B. D., & Shull, J. M. 2012, ApJ, 748, 12
Smith, N. 2007, AJ, 133, 1034
Smith, N., Arnett, W. D., Bally, J., Ginsburg, A., & Filippenko, A. V. 2013, MNRAS, 429, 1324
Smith, N., Zhekov, S. A., Heng, K., et al. 2005, ApJL, 635, L41
Sonneborn, G., Pun, C. S. J., Kimble, R. A., et al. 1998, ApJL, 492, L139
Sugerman, B. E. K., Crotts, A. P. S., Kunkel, W. E., Heathcote, S. R., & Lawrence, S. S. 2005, ApJS, 159, 60
Telesco, C. M., Pina, R. K., Hanna, K. T., et al. 1998, Proc. SPIE, 3354, 534
Thatte, N. A., Tecza, M., Eisenhauer, F., et al. 1998, Proc. SPIE, 3353, 704
Walborn, N. R., Phillips, M. M., Walker, A. R., & Elias, J. H. 1993, PASP, 105, 1240
Walker, A. R., & Suntzeff, N. B. 1990, PASP, 102, 131
Wampler, E. J., Wang, L., Baade, D., et al. 1990, ApJL, 362, L13
Wang, L., D'Odorico, S., Gouiffes, C., et al. 1992, IAUC, 5449
Werner, M. W., Roellig, T. L., Low, F. J., et al. 2004, ApJS, 154, 1
Wood, P. R., Faulkner, D. J., Couch, W. J., & Malin, D. F. 1989, IAUC, 4739
Wright, G. S., Rieke, G. H., Glasse, A., et al. 2023, PASP, 135, 048003